Electronic Supplementary Information†

Dynamic Competitive Strains Enabled Self-Supporting Janus Nanostructured Films for High-Performance Airflow Perception

Wei Zhou,[a,b] Peng Xiao,*[a,b] Chang Zhang,[a,b] Qing Yang,[c,d] and Tao Chen*[a,b]

[a]Key Laboratory of Marine Materials and Related Technologies, Zhejiang Key Laboratory of Marine Materials and Protective Technologies, Ningbo Institute of Materials Technology and Engineering, Chinese Academy of Sciences, Zhongguan West Road 1219, Ningbo 315201, China.

[b]School of Chemical Sciences, University of Chinese Academy of Sciences, 19A Yuquan Road, Beijing 100049, China.

*Corresponding author, Email: xiaopeng@nimte.ac.cn; tao.chen@nimte.ac.cn

[c]State Key Laboratory of Modern Optical Instrumentation, College of Optical Science and Engineering, International Research Center for Advanced Photonics, Zhejiang University, Hangzhou 310027, China

[d]Research Center for Intelligent Sensing, Zhejiang Lab, Hangzhou 311100, China

KEYWORDS: Janus nanostructured hybrid film, self-supporting, dynamic strains competition, ultrasensitive airflow sensing, wide-range detection

Experimental Section

Materials

Carbon spheres nanoparticles (diameter ≈ 50 nm) were purchased from the Nafudis Technology Co., Ltd. The graphene raw material is a slurry with a solid content of 5 *wt*%, which was produced by Ningbo Institute of Material Technology and Engineering, Chinese Academy of Sciences, relying on Ningbo Morsh Technology Co., Ltd. It is stored under a vacuum immediately after each use to ensure the solid content remains unchanged. The commercial Ecoflex 00-50 silicon rubber is used as the elastic matrix, which is purchased from Smooth-on, USA. Other analytical reagent grade solvents and reagents, *e.g.*, anhydrous ethanol and n-heptane were obtained from Sinopharm Chemical Reagent Co., Ltd.

Preparation of GCH film

Firstly, an appropriate amount of graphene and carbon spheres hybrids with a certain weight ratio were dispersed in anhydrous ethanol, followed by an ultrasonic treatment (250 W) for six hours to obtain a relatively stable and uniform dispersion. Subsequently, the preassembled graphene and carbon spheres hybrid (GCH) film was formed on the water/air interface by a typical spray coating method with an appropriate volume of dispersion. In this stage, the Marangoni effect-induced assembly behavior only forms a relatively loose structure in the hybrid film. After that, the preassembled film was left for half an hour to allow complete evaporation of ethanol and stabilization of the internal structure. A commercial porous sponge was adopted to squeeze along one side, driving the preassembled film to form a condensed structure. In this process, the siphoning effect-induced effective absorption of water destroyed the force equilibrium of the preassembled film at the water surface, resulting in a rapid compression towards the reverse direction. Finally, the uniform GCH film with a closely packed structure was

formed on the water/air interface. It is worth noting that the hybrid ratio of the graphene and carbon spheres in the suspension and the concentration of the GCH dispersion can be adjusted, respectively. Thus, the microstructure inside the material can be effectively regulated to achieve optimal sensing performance.

Preparation of GCEF

First, component A and B of the Ecoflex were dissolved in n-hexane and sonicated for five minutes to form a homogeneous solution (14 *wt*%). Then, the resulted solution was dropwise dripped onto the GCH film surface along the edge and it spread uniformly across the water/air interface through the diffusion effect. After curing at room temperature for six hours, the elastic and uniform GCEF was obtained at the water/air interface.

Fabrication of the GCEF-based airflow sensor and the AISW array

First, a piece of flexible PET commercial film rinsed with anhydrous ethanol was conformally attached to the Ecoflex side of the GCEF at the water/air interface. To ensure the conformal attachment of GCEF on PET, the transfer process was carried out by first attaching one side of PET to the GCEF surface and then slowly releasing the other parts along the already attached portion. Afterward, the GCEF was successfully transferred to the PET surface by cutting the surrounding edges of the unattached region. After removing the interlayered water to form a relatively tight contact between the film and the PET surface at room temperature, the GCEF was cut into stripes with the size of 0.2 × 5 cm. It should be noted that if the GCEF was dried by heating, the adhesion between the GCEF and the PET film would be too strong for the stripes to be detached easily. The released GCEF stripes were then fixed to the hollow PLA frame by double-sided adhesive with the self-supported portion of 3 cm in length. Finally, the electrodes were adhered to the fixed ends on both sides and encapsulated with PDMS. Thus, the

GCEF-based airflow sensor with the self-supporting configuration was fabricated successfully. As for the AISW array, the only difference is that the hollow PLA frame was replaced by a 3D printed spiderweb pattern. The length of the self-supporting part was still maintained at 3 cm, and the eight stripes were distributed in a circular pattern at 45° intervals from each other.

Airflow sensing performance test

The current-time curve and the current-voltage curve of the GCEF-based airflow sensor were tested by an electrochemical workstation (CH Instruments, CHI660E.Chenhua Co., Shanghai, China) with an input voltage of 1V. To accurately measure changes in conductivity, an air tube adjusted to a certain flow rate was loaded vertically above the sensor and the airflow was controlled on/off by pulling back and forth on the plastic piece between the sensor and the air tube (Fig. S18). For the AISW array, the real-time current of the eight sensors was collected by eight commercial high-precision ammeters (TDM2001P, HangZhou TESOO Technology Co., Ltd). The airflow velocity (v) was calculated by the following formula (1):

$$v = \frac{Q}{S} \tag{1}$$

where Q is the flow flux of the high-purity nitrogen, which can be read directly from the commercial gas mass flowmeter (MF5712) and S is the cross-sectional area of the air tube.

Finite element simulation of the deformation behavior and strain distribution of the GCEF stripe

The model for the finite element simulation was built based on actual experimental conditions. The dimensions of the stripe were 50 × 2 × 0.1 mm. The length and width were measured directly by vernier calipers, while the thickness was estimated from the cross-sectional

SEM images of the GCEF. The self-supporting part of the stripe is 30 mm, leaving 10 mm at each end for fixing the whole stripe. The density and Poisson's ratio of the stripe were calculated as 1.23 g cm^{-3} and 0.3, respectively, and the modulus of elasticity was calculated as 425 kPa from the slope of the stress-strain curve of the stripe in the interval 0-50% (Fig. S4). A linear elastic material model was used for the whole simulation process. The airflow was applied vertically in the middle of the stripe and the distance was about 4 mm away from the film surface. The airflow was loaded according to uniform acceleration followed by uniform velocity. After the airflow is stabilized, the displacement of GCEF in the longitudinal direction and the strain distribution in the transverse plane were calculated.

Characterization

The surface and cross-sectional micromorphology of the GCH film and the GCEF were obtained with the cold field emission scanning electron microscope (FE-SEM) at an accelerating voltage of 4 kV (Hitachi S4800). The cross-sectional element distribution of the GCEF was performed with the cold field high-resolution scanning electron microscope (10 kV, Regulus 8230) and the energy spectrum analyzer (XFlash 6/100) at the line scan mode. The Raman spectra were collected by R-3000HR spectrometer (Raman Systems, Inc., R-3000 series) using a solid-state diode laser (532 nm) as the excitation source in the frequency range of 3500–300 cm^{-1}. The stress-strain curve was tested by the universal material testing machine at a tensile rate of 50 mm/min (Zwick Z1.0).
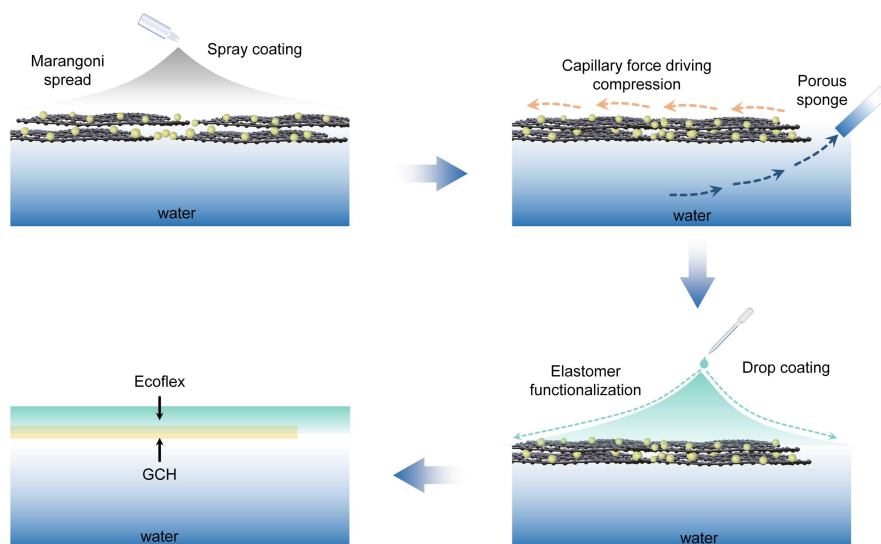
Fig. S1. Schematic of the construction for GCEF. In detail, it includes the self-assembly of GCH based on Marangoni effect, capillary force driving compression of preassembled film assisted with porous sponge and asymmetric functionalization with Ecoflex.
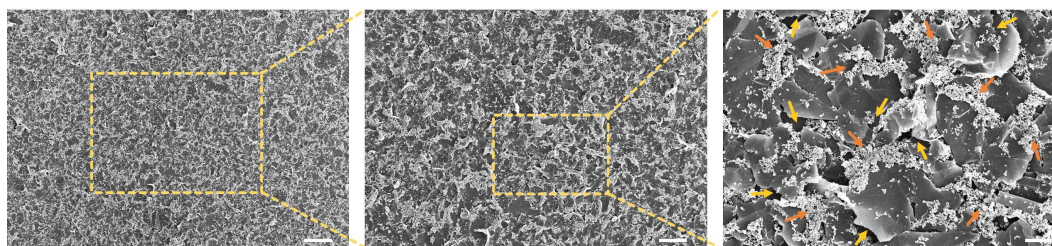

Fig. S2. Surface morphologies of GCH at different magnifications. The orange and yellow arrows indicate carbon spheres clustered at the edges of the graphene lamellae and voids on the GCH surface, respectively. The scale bar is 20 μm, 10 μm, and 2 μm, respectively.
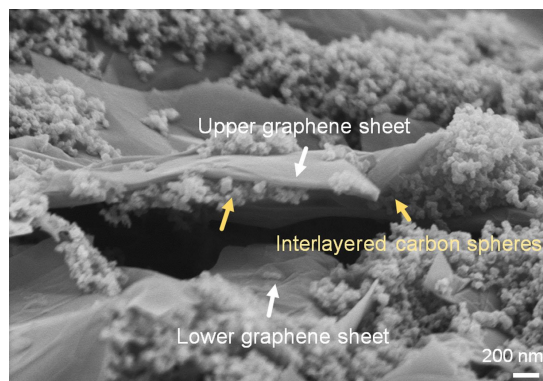
Fig. S3. The cross-sectional SEM image of GCH.
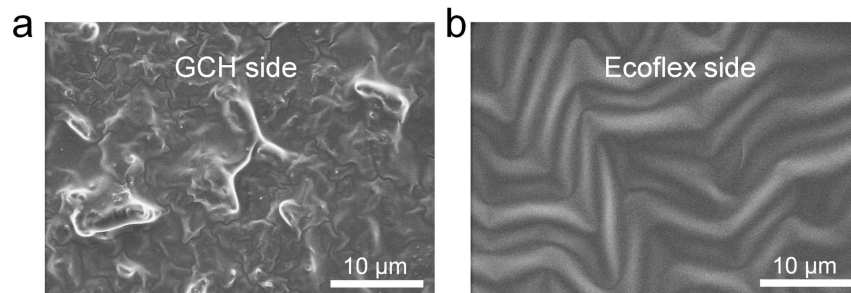
Fig. S4. Characterization of the asymmetric surface morphology at both sides in GCEF. SEM images of the GCH side (a) and Ecoflex side (b).
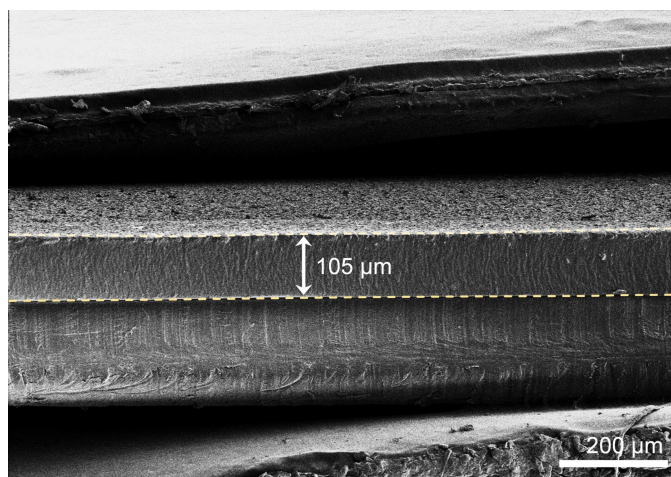
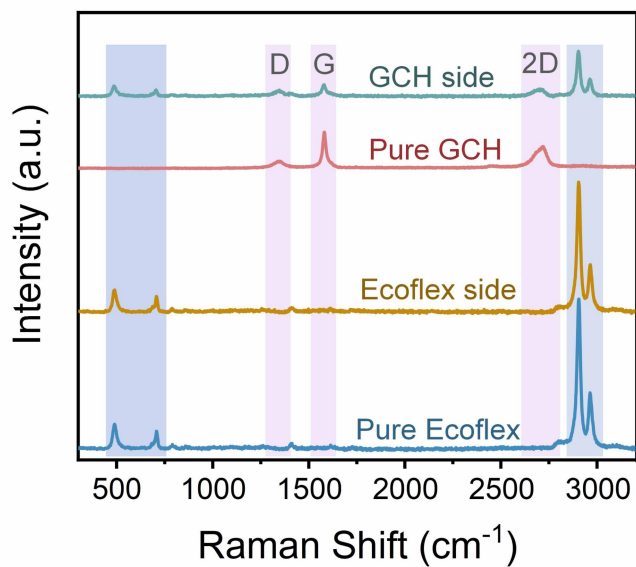**Fig. S5.** Cross-sectional SEM image of the GCEF.
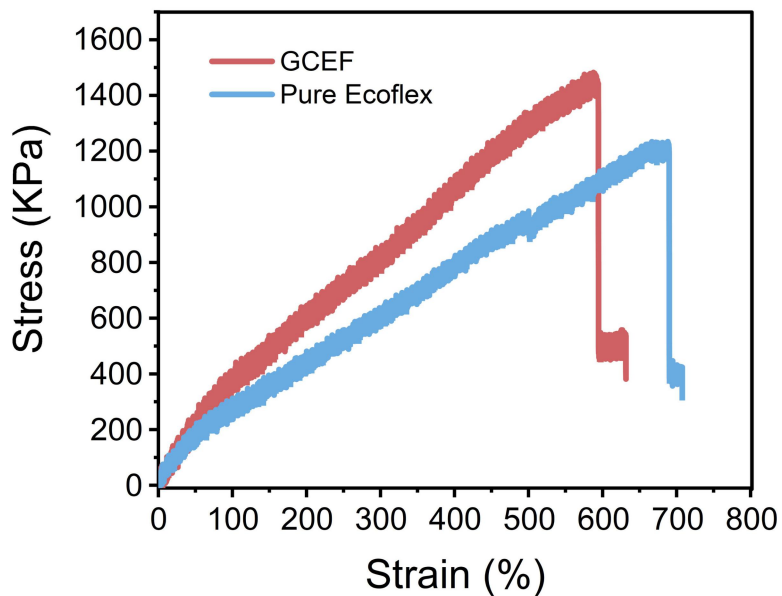
Fig. S6. The stress versus strain curves of the GCEF and pure Ecoflex. The size of the stretched sample is about $50 \times 2 \times 0.1$ mm, where 10 mm is left at each end for clamping the sample strip.
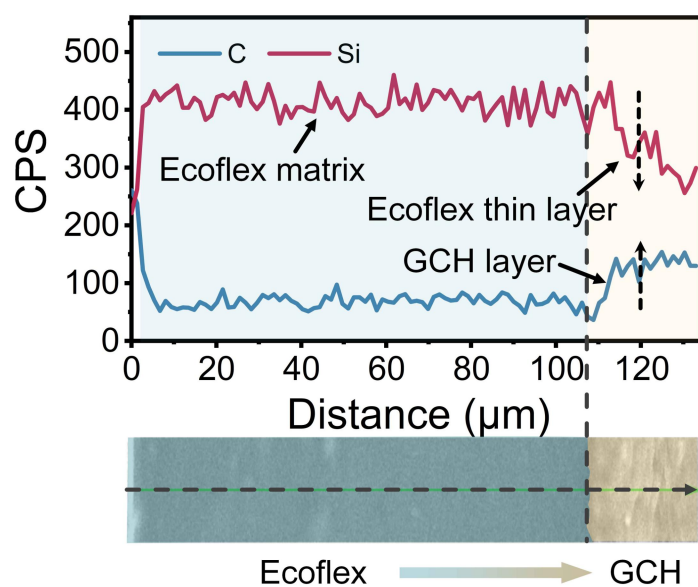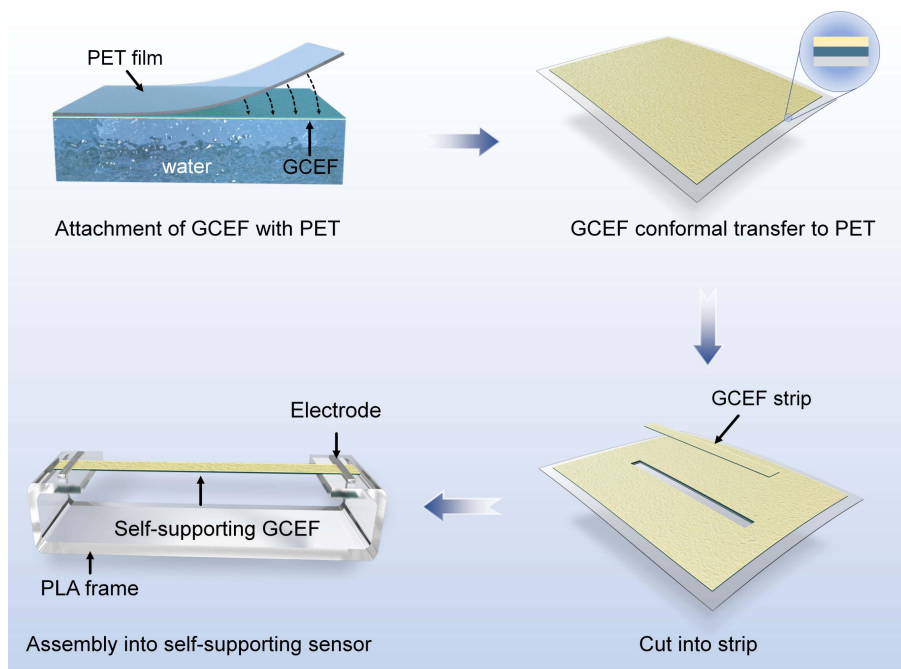

Fig. S7. EDS characterization. The element distribution along the cross-section of the GCEF scanning from the Ecoflex side to GCH side.
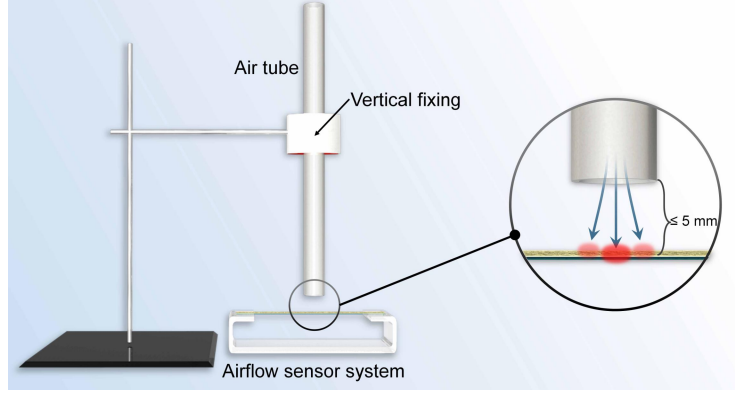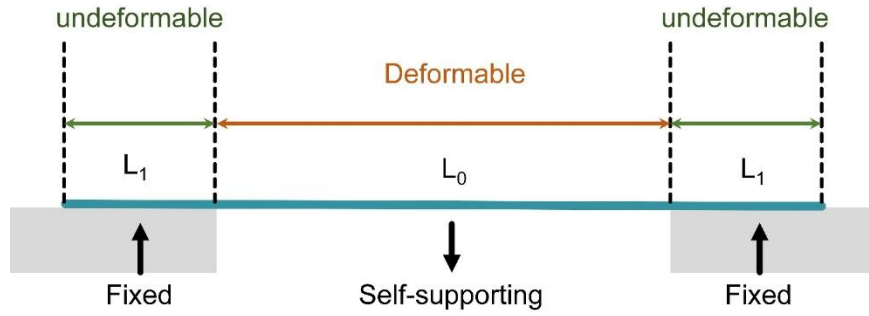
Fig. S8. Raman spectroscopy characterization. Raman spectra of the pure GCH film, pure Ecoflex, the GCH and Ecoflex side of the GCEF.

Fig. S9. Schematic of the fabrication for the self-supported GCEF-based airflow sensor.

Fig. S10. Schematic diagram of the deformation test setup for GCEF stripe.

Fig. S11. Schematic illustration of the dimensions in deformable and undeformable regions. Among them, $L_0 = 3$ cm, and $L_1 = 1$ cm.

Where, the average strain (ε'_T) in the transverse direction was calculated from the finite element simulation results, which includes the whole self-supporting part and the fixed part of the strip. Therefore, according to the definition of strain, ε'_T can be expressed by Equation (2) when there is a deformation of ΔL:

$$\varepsilon'_T = \frac{\Delta L}{2L_1 + L_0} \tag{2}$$

However, since it is mainly the self-supporting part that deforms under the airflow stimulus, the transverse average strain (ε_T) including only the self-supporting part was recalculated according to the following Equation (3) in order to minimize the calculation error.

$$\varepsilon_T = \frac{\Delta L}{L_0} \tag{3}$$

Thus, ε_T can be calculated from Equation (2) and (3), as shown in Equation (4):

$$\varepsilon_T = \varepsilon_T' \frac{2L_1 + L_0}{L_0} \tag{4}$$

In general, the Poisson's ratio of a material is a constant value when the ambient temperature is determined. Therefore, the longitudinal strain (ε_L) in the whole deformation process can be deduced from the definition of Poisson's ratio (μ) in Equation (5):

$$\mu = -\frac{\varepsilon_L}{\varepsilon_T} \tag{5}$$

Therefore, ε_L can be calculated from Equation (4) and (5), as shown in Equation (6):

$$\varepsilon_L = -\mu \, \varepsilon_T' \frac{2L_1 + L_0}{L_0} \tag{6}$$

All the strains (ε_T', ε_T, ε_L) calculated from the above equations are summarized in Table S1.
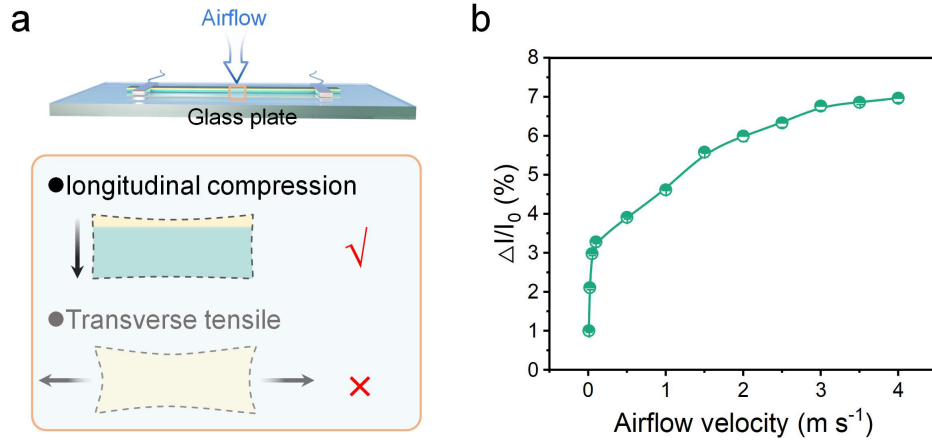

Fig. S12. The airflow sensing performance with the constrained transverse strain. (a) Schematic of airflow response test with GCEF attached to a glass plate, in which the transverse strain is absent due to the constraint of the rigid substrate. (b) Relative current variation *versus* airflow velocity curve for the transversely constrained GCEF.
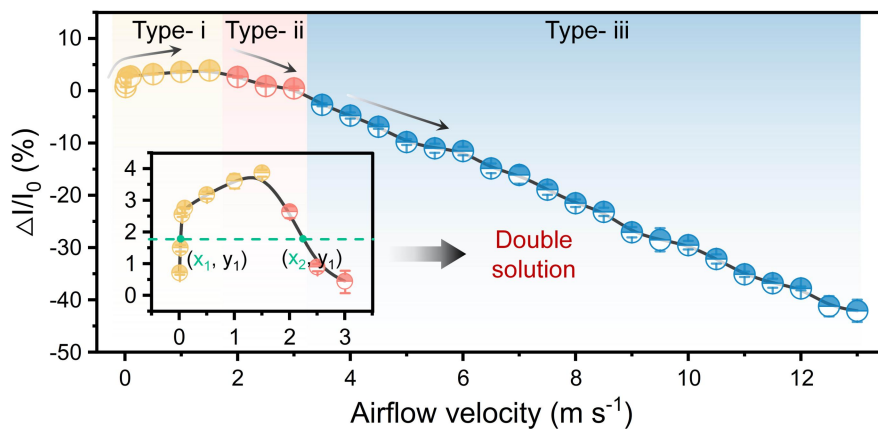
Fig. S13. The normalized current versus airflow velocity curve. Stage-i, ii, and iii correspond to the curves of type-i, ii, and iii, respectively. Inset: Double solution phenomenon existed in stage-i and stage-ii (test number, n = 3).
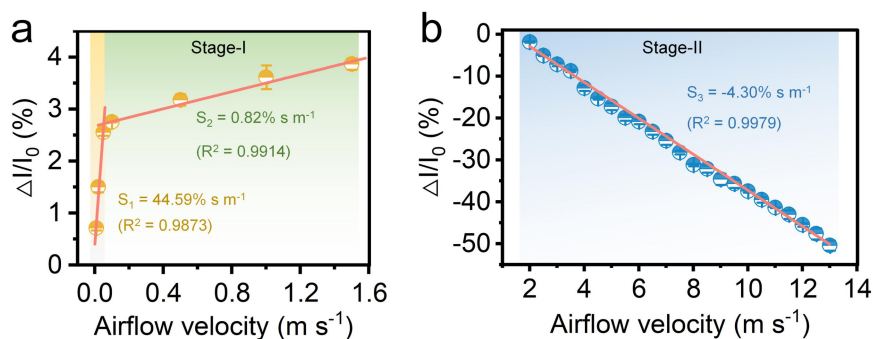

Fig. S14. The sensitivity of the sensor in two stages. The relationship between the relative current variation and airflow velocities in stage-I (a) and II (b). The sensitivity was calculated from the slope of the linear fitting curves.
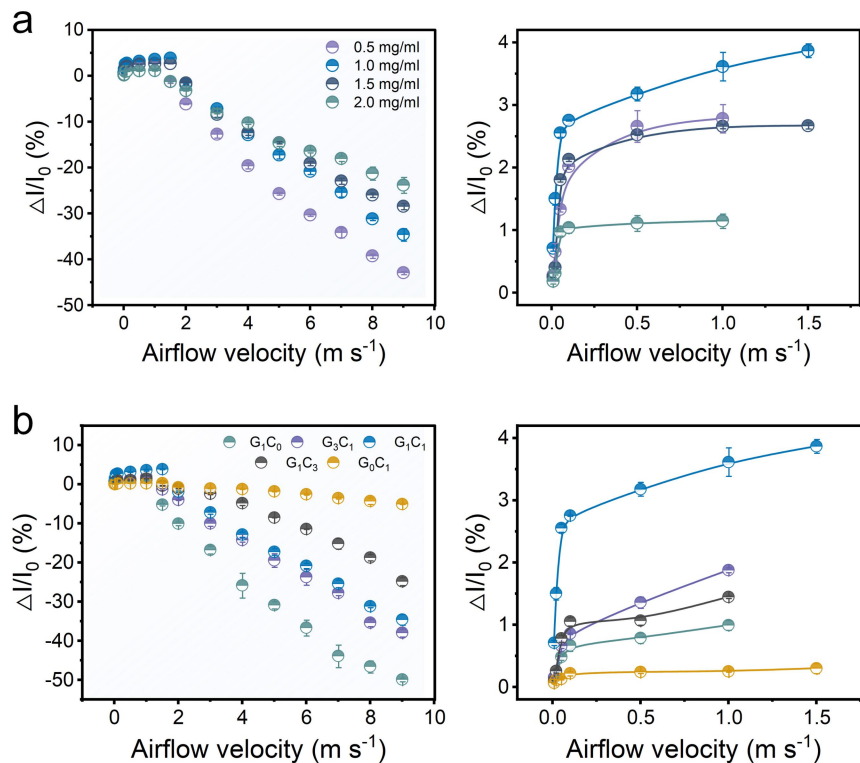
Fig. S15. The influence of the concentration and hybrid ratio of the GCH layer on the sensing performance. The relative current variation curve at different graphene concentrations (a) and different hybridization ratios (b) of graphene and carbon spheres.
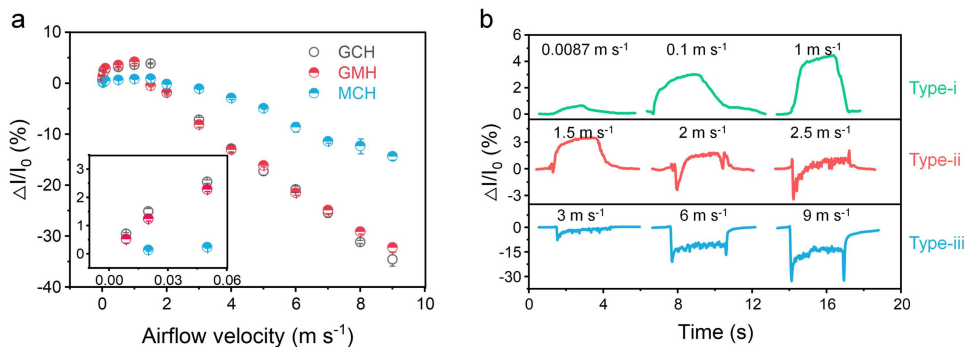

Fig. S16. The airflow response performance of hybrid materials with different dimensions. (a) The relative current variation curves of GCH, GMH, and MCH, where GMH and MCH represent graphene/multi-walled carbon nanotube hybrid and multi-walled carbon nanotube/carbon sphere hybrid, respectively. (b) Three types of current curve characteristics of GMH under different airflow velocities.
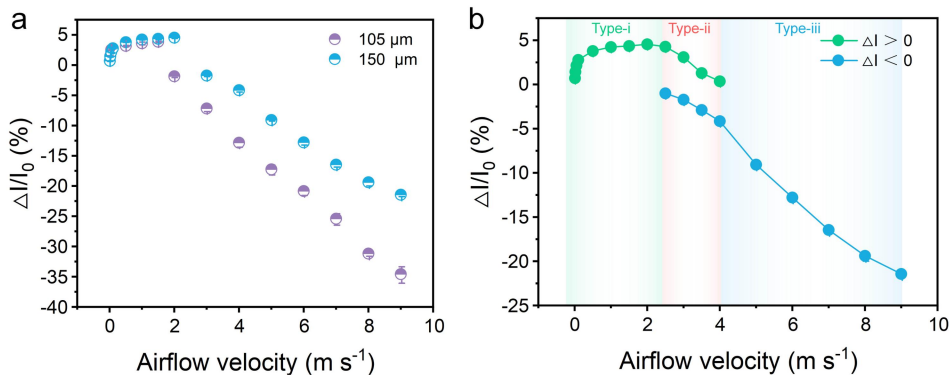
Fig. S17. The effect of thickness on the airflow response performance. (a) The relative current variation curves of GCEF with different thicknesses. (b) The trend of maximum current variation for the GCEF with a thickness of ~150 μm.
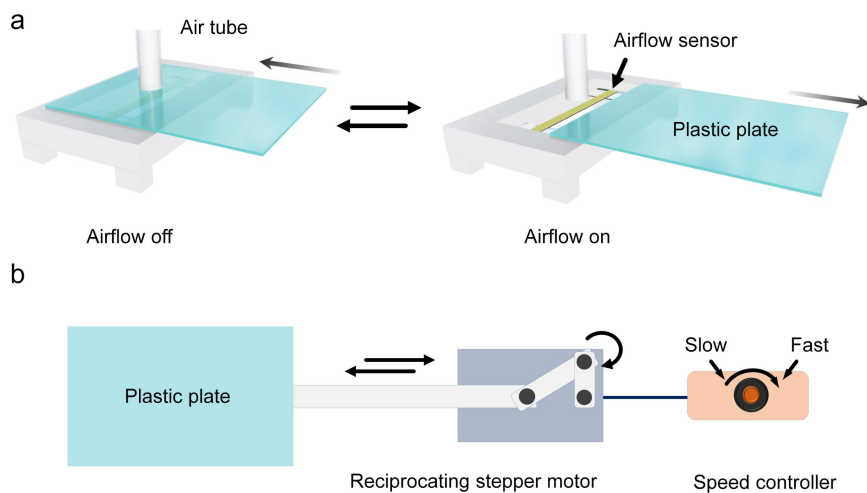

Fig. S18. Schematic of frequency response performance test. (a) Diagram of the control for airflow switch. In this case, the switching behavior of airflow is controlled by pulling the plastic sheet back and forth. When the plastic sheet is pulled away to expose the airflow sensor, the airflow state is on, and conversely, it is off. (b) Illustration of the device for accurate control of airflow switching frequency. Where, the plastic sheet is directly connected to the reciprocating stepping motor, whose speed of back-and-forth linear movement is regulated by the speed controller. Therefore, well control of the airflow switching frequency is finally achieved.
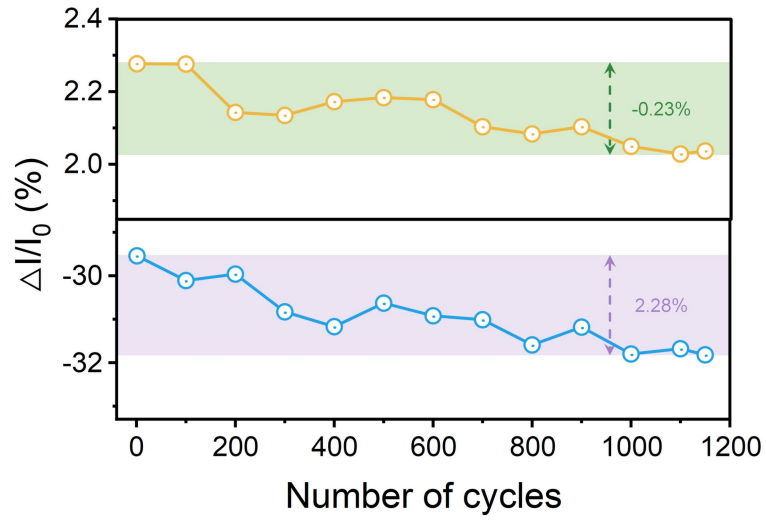
Fig. S19. The relationship between the maximum current variation and the number of airflow cycles stimulation.
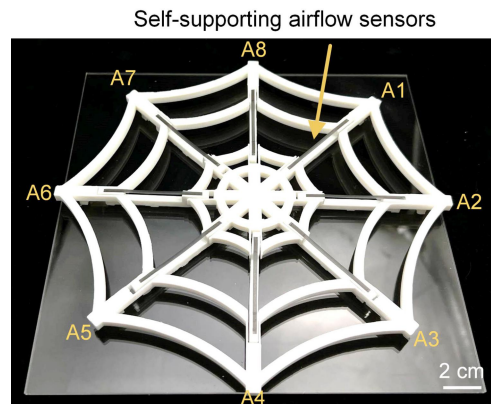
Fig. S20. Photo of a homemade AISW consisting of eight self-supporting airflow sensors.
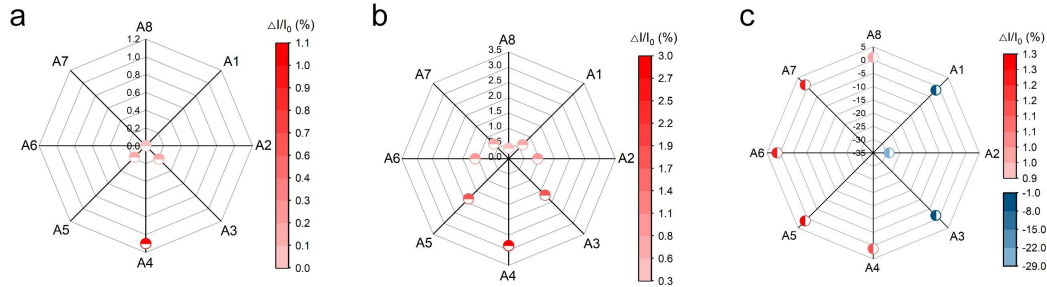
Fig. S21. Identifying the intensity and location of the applied airflow with AISW array. Distribution of relative current change for each sensor in the AISW array at different airflow intensities and stimulus locations. (a) 0.02 m s^{-1}, A4. (b) 1 m s^{-1}, A4. (c) 7.5 m s^{-1}, A2.
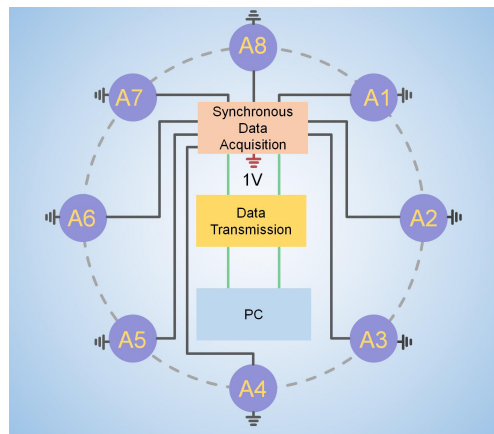
Fig. S22. Circuit connection sketch for the AISW system. Here, the real-time current of the eight sensors in the array are collected by eight high-precision ammeters, and the CH340 communication module is used to transfer the obtained data to the python software in the computer for analysis, and the final processing results are transferred to the processing software in the computer to control the animation display.
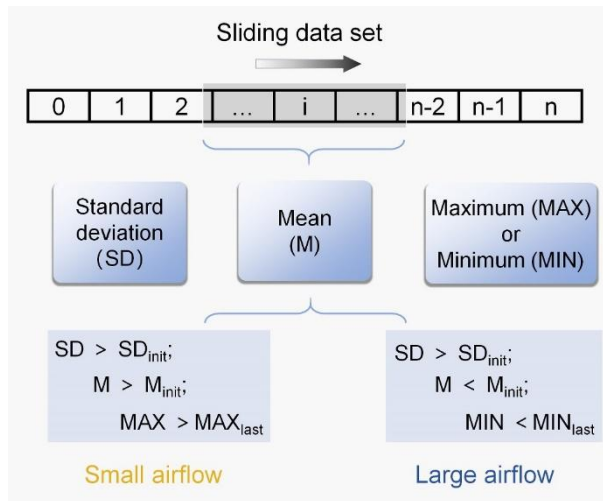
Fig. S23. Schematic of the principle for the airflow stage identification.
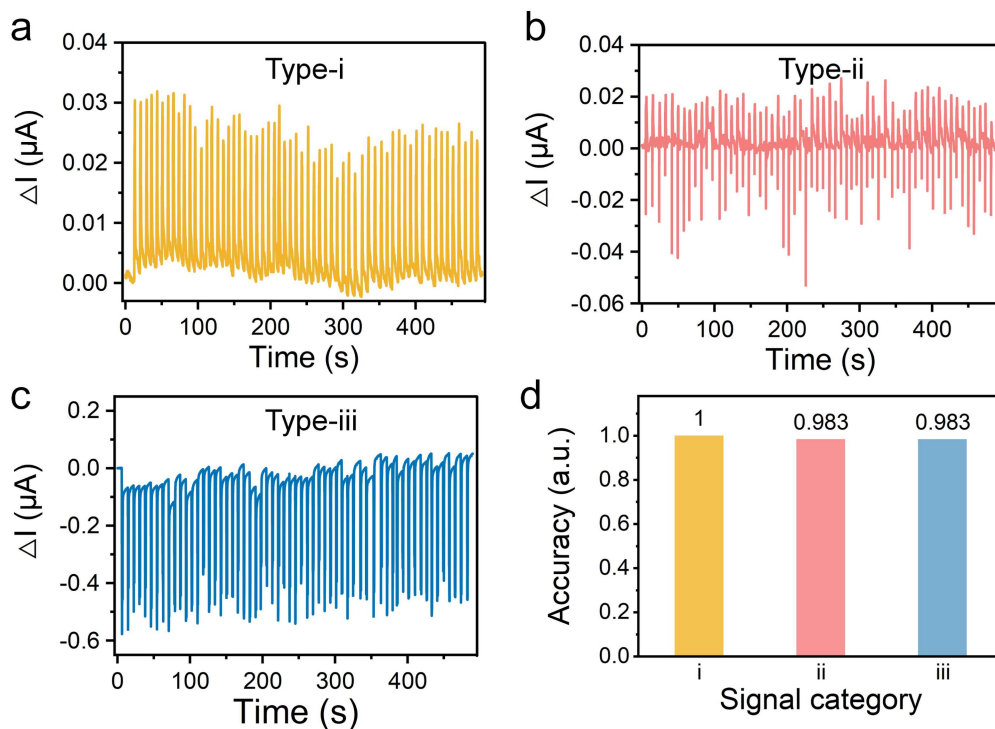
Fig. S24. Characterization of airflow stages recognition ability under 60 airflow cycles stimulation. (a-c) Three types of current curves recorded in real time at 1.09, 1.85, and 5.8 m s^{-1}, respectively. (d) The recognition results with high accuracy for all current curves.

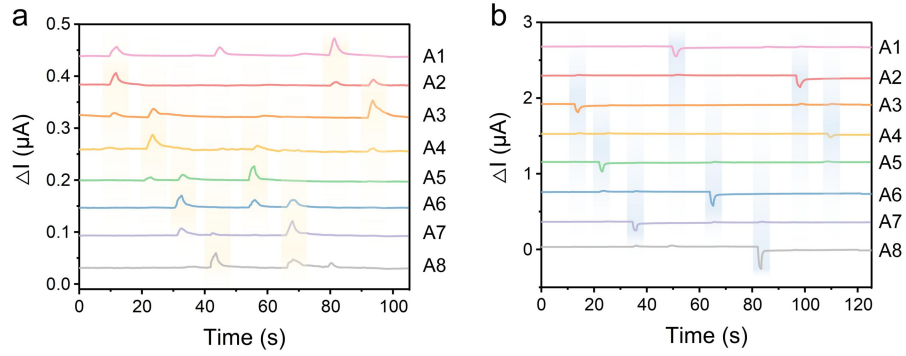**Fig. S25.** The current signals of the AISW when the airflow acts randomly. The filtered current signals of each sensor in the AISW array when stimulating the array in the random order at the velocity of 0.79 m s^{-1} (a) and 2.75 m s^{-1} (b).
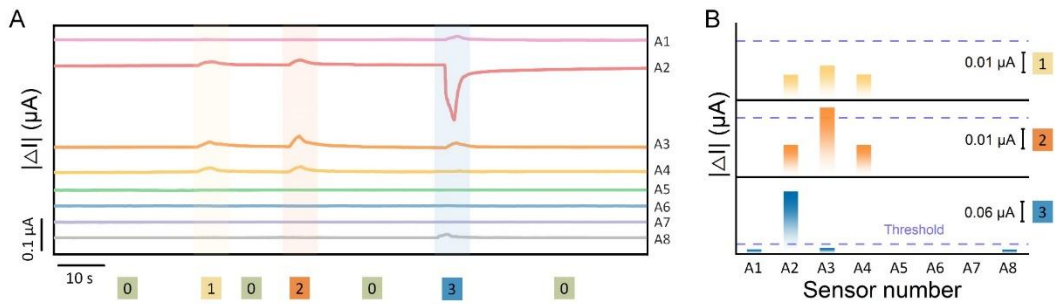
Fig. S26. The collected current signals of the AISW when stimulating different positions in the AISW array with different intensities of airflow. (a) The filtered current variation of each sensor in the AISW array. (b) Comparison of the absolute value of the maximum current change and the threshold value for each sensor.

Table S1. ε'_T, ε_T, and ε_L summarized from simulation results and Poisson's ratio equation.

Airflow velocity (m s^{-1})	ε'_T (%)	ε_T (%)	ε_L (%)
0.0087	0.0012535	0.00208917	0.0006268
0.05	0.0064559	0.01075983	0.003228
1.0	0.98332	0.1638867	0.049166
1.5	0.12693	0.21155	0.063465
2.0	0.23667	0.39445	0.118335
5.0	0.7947	1.3245	0.39735
10	1.948	3.2467	0.974
13	2.7355	4.559167	1.36775

Table S2. Sensing performance of our airflow sensor with other reported airflow sensors based on various sensing principles.

Materials	Principle	Detection limit	Detection range	Response time	Ref.
Al and Pt wires	Hot wire	0.01 m s^{-1}	0.01 - 17.5 m s^{-1}	0.3 s	1
Ni/W multilayer thin film	Hot wire	0.5 m s^{-1}	0.5 - 30 m s^{-1}	N/A	2
Pt wires	Hot wire	0.3 m s^{-1}	0.3 - 6 m s^{-1}	0.1 s	3
Ti/Pt	Hot film	0.1 m s^{-1}	0.1 - 10 m s^{-1}	N/A	4
Microsphere-tipped PDMS micropillars	Optical	0.04 m s^{-1}	0.04 - 0.15 m s^{-1}	N/A	5
Metal-core Piezoceramic Fiber	Piezoelectric	0.05 m s^{-1}	0.05 - 10 m s^{-1}	N/A	6
PVDF fiber with a molybdenum core	Piezoelectric	~2.5 m s^{-1}	~2.5 - 14 m s^{-1}	N/A	7
RGO	Electrical	0.026 m s^{-1}	0.026 - 7.2 m s^{-1}	26 s	8
Carbon nanotubes and silver nanoparticles composite film	Piezoresistance	~1.25 m s^{-1}	~1.25 - 3 m s^{-1}	0.1 s	9
CNT/PDMS	Piezoresistance	0.5 m s^{-1}	0.5 - 7 m s^{-1}	N/A	10
PTFE film	Piezoresistance	6.5 m s^{-1}	6.5 - 10.8 m s^{-1}	N/A	11
Au/Doped Si	Piezoresistance	2 m s^{-1}	2 - 20 m s^{-1}	~ 2 s	12
Nylon fibers/carbonized paper	Piezoresistance	11.5 m s^{-1}	11.5 - 43.7 m s^{-1}	0.7 s	13
CNTs/CSF	Piezoresistance	0.05 m s^{-1}	0.05 - 7 m s^{-1}	1.3 s	14
SiNW	Piezoresistance	0.15 m s^{-1}	0.15 - 15.3 m s^{-1}	0.04 s	15

CFS/PVA fiber	Piezoresistance	0.068 m s^{-1}	0.068 - 16 m s^{-1}	0.103 s	16
SCNTNs	Piezoresistance	0.11 m s^{-1}	0.11 - 5.51 m s^{-1}	0.021 s	17
GCEF	**Piezoresistance**	**0.0087 m s^{-1}**	**0.0087 - 23 m s^{-1}**	**1.5 s (0.0087 – 1.5 m s^{-1}) 0.12 s (1.5 – 23 m s^{-1})**	**This work**

Reference

1   M. M. Sadeghi, R. L. Peterson and K. Najafi, *J. Micromech. Microeng.*, 2013, **23**, 085017.

2   A. Talbi, L. Gimeno, J.-C. Gerbedoen, R. Viard, A. Soltani, V. Mortet, V. Preobrazhensky, A. Merlen and P. Pernod, *J. Micromech. Microeng.*, 2015, **25**, 125029.

3   S. Zhao and R. Zhu, *Adv. Mater.*, 2017, **29**, 1606151.

4   H.-B. Liu, N. Lin, S.-S. Pan, J. Miao and L. K. Norford, *IEEE Sensors J.*, 2013, **13**, 1914–1920.

5   J. Paek and J. Kim, *Nat. Commun.*, 2014, **5**, 3324.

6   Y. Bian, Y. Zhang and X. Xia, *J Bionic Eng*, 2016, **13**, 416–425.

7   Y. Bian, R. Liu and S. Hui, *Funct. Mater. Lett.*, 2016, **9**, 1650001.

8   Z. Xu, K. Wu, S. Zhang, Y. Meng, H. Li and L. Li, *Mater. Horiz.*, 2017, **4**, 383–388.

9   K. Takei, Z. Yu, M. Zheng, H. Ota, T. Takahashi and A. Javey, *Proc. Natl. Acad. Sci. U.S.A.*, 2014, **111**, 1703–1707.

10   J. Park, Y. Lee, J. Hong, M. Ha, Y.-D. Jung, H. Lim, S. Y. Kim and H. Ko, *ACS Nano*, 2014, **8**, 4689–4697.

11   H. Guo, J. Chen, L. Tian, Q. Leng, Y. Xi and C. Hu, *ACS Appl. Mater. Interfaces*, 2014, **6**, 17184–17189.

12   H. Takahashi, A. Nakai and I. Shimoyama, *Sens. Actuator A Phys.*, 2018, **281**, 243–249.

13   Y.-F. Liu, P. Huang, Y.-Q. Li, Q. Liu, J.-K. Tao, D.-J. Xiong, N. Hu, C. Yan, H. Wang and S.-Y. Fu, *J. Mater. Chem. A*, 2019, **7**, 1889–1896.

14   H. Wang, S. Li, Y. Wang, H. Wang, X. Shen, M. Zhang, H. Lu, M. He and Y. Zhang, *Adv. Mater.*, 2020, **32**, 1908214.

15   S. Huang, B. Zhang, Y. Lin, C.-S. Lee and X. Zhang, *Nano Lett.*, 2021, **21**, 4684–4691.

16   J. Luo, N. Ji, W. Zhang, P. Ge, Y. Liu, J. Sun, J. Wang, Q. Zhuo, C. Qin and L. Dai, *Mater. Horiz.*, 2022, **9**, 1503–1512.

17   Q. Jiang, R. Li, F. Wang, X. Shi, F. Chen, Y. Huang, B. Wang, W. Zhang, X. Wu, F. Wei and R. Zhang, *Adv. Mater.*, 2022, **34**, 2107062.